Journal of Engineering Mathematics **45:** 309–334, 2003.

Fluid motion for car undertrays in ground effect

M.A. JONES and F.T. SMITH
Department of Mathematics, University College London, Gower Street, London WC1E 6BT, U.K.

Received 15 February 2002; accepted in revised form 31 October 2002

Abstract. Air motion representative of some of the flows past a moving car is studied, particularly in the gap between the car underbody (undertray, front flap or forewing) and the ground, using theory and computation. The ground-affected flows encountered are two- or three-dimensional, laminar, transitional or turbulent, and attached or separated. Given Reynolds numbers in the approximate range 1–10 million, emphasis here is placed first on key physical flow mechanisms: viscous-inviscid interaction filling either much or part of the gap; the generation of strong upstream influence; an abrupt pressure jump at the leading edge; the moving-ground condition; substantial diffuser flow reversals and wake effects; in three dimensions the distinguishing between inflow and outflow edges; and turbulent flow modelling. Second, for various underbody shapes, predictions are presented of the surface pressures and shear stresses, the lift or downforce, and the velocity profiles. Extensions of these to include edge effects, three-dimensionality and turbulence modelling are examined, along with optimization for certain shapes concerned with front-flap design and comparisons with recent experiments.

Key words: cars, downforce, flaps, ground effects

1. Introduction

The present theoretical and computational research is on the physical description and modelling of basic effects, due to a car underbody (undertray, front flap, front diffuser/wing or forewing) and to the presence and relative movement of the ground (the ground effect), on the air flow past a car. This is especially in the comparatively narrow gap between the underbody and the ground. The motivation and corresponding aim of the modelling concern in particular the underbody shaping effects and their influence on lift (or downforce) distribution and drag, through the induced shear stresses and pressures at the undersurface. In practice, an underbody shape that produces a minimum gap clearance near the front (leading edge) of the vehicle and gentle divergence of the gap thereafter, for example, tends to induce a beneficial downforce near the leading edge but with the disadvantage of an adverse pressure gradient towards the vehicle rear (trailing edge) which can cause separation of the air flow.

The flow in reality is complex, three-dimensional, unsteady and probably turbulent for the most part; see computations and experiments described in [1-10]. On the other hand, relatively little research of a theoretical nature appears to have been done on all the fundamental flow mechanisms involved in the present underbody-to-ground interactions, although very significant contributions on various related aspects are by [11–18] and early internal-flow interaction studies *e.g.* [19,20] are also relevant. Accordingly, it seems sensible as a first basic step to tackle the incompressible range of two-dimensional steady laminar motions and subsequently consider the added complexities of three-dimensionality, turbulence and so on; this is the present plan. In similar vein thin bodies (representative of cars) are considered first, followed by thicker ones. Wheels and their influence on underbody flows are discounted.

The work is directed at the intriguing aspects of two- and three-dimensional air motion past cars and other such vehicles (*e.g.* wings in ground effect) which are distinct from conventional aerodynamics [10, Chapter 5].

The emphasis here is on several physical mechanisms that act in the underbody-to-ground gap flows. These involve, in the two-dimensional setting, viscous-inviscid coupling, the pressure response to a fixed clearance/displacement (or vice-versa in a design mode), the trailing edge constraint, strong upstream influence, an abrupt pressure jump focussed at the leading edge, the moving ground condition, and substantial flow separations, while in the three-dimensional setting at least three more flow mechanisms are found to arise. Some of these flow mechanisms are well known already, some less so or not at all. In particular, viscous-inviscid interaction is taken to fill the whole of the gap flow or a substantial part of it. This filling or partial filling is an important factor because (unlike inviscid theory) it not only provides the capability of treating flow reversals/separations in a regular fashion but also accommodates the substantial influences of the moving ground condition.

The Reynolds number Re based on body length and speed is assumed to be large. For a vehicle of length 3 metres [300c.g.s.], say, travelling at speed 50–200 km/hour [14–56 $\times 10^2$ c.g.s.], and with a representative kinematic viscosity of $0{\cdot}19$ cm^2/sec for air, the value of Re is in the range $2{\cdot}2$–$8{\cdot}8 \times 10^6$. Hence δ, the typical boundary-layer thickness measured relative to the vehicle length, lies approximately in the range $3{\cdot}4$–$6{\cdot}7 \times 10^{-4}$ deduced from the scale $\mathrm{Re}^{-\frac{1}{2}}$ for laminar flow and 6–7 $\times 10^{-2}$ for turbulent flow deduced from the deficit layer scale $1/\log \mathrm{Re}$ rather than the displacement or momentum thickness.

The relative thickness δ, although based only on attached-flow estimates, can usefully be compared with the ratio H of the typical gap clearance (say 2–20 cms.) to the vehicle length, the ratio H being $6{\cdot}7$–67×10^{-3}. So the gap tends to be thicker than the nominal attached laminar boundary layer by a factor of from 5 to 200, whereas the attached turbulent boundary layer thickness exceeds the above gap clearance by a factor of about 1 to 10. The approximate comparability here adds some weight to the supposition that viscous-inviscid forces may fill a significant portion of the gap flow. Furthermore, the decrease of Re at lower vehicle speeds increases δ, making the laminar case more closely comparable, as well as more likely to occur in practice then. The same trend comes from flow separation, for instance on approach to the gap trailing edge, provoking boundary layers substantially thicker than in the numerical estimates above, as we shall see later in this paper. This trend towards viscous-inviscid filling is also accentuated by design developments with much reduced gap clearances especially near the leading edge, in high-performance racing cars for example, to lower the pressure and increase the downforces for traction.

The above trends point overall to application of the (interactive) boundary layer system to account for the whole narrow gap flow. The gap ratio H being small almost immediately suggests application of a thin-layer approximation and this, with viscous effects added, yields the interactive boundary layer system, capturing the influences of separation and the moving ground. The system provides a unified treatment, incorporating flow separation, viscous-inviscid counterbalances and the ground movement, as well as allowing where necessary for the relative thickness or thinness of the gap (H) compared with the typical laminar or turbulent flow thickness (δ) respectively.

The laminar case is considered in Sections 2–5 below, with a start on the turbulent case being addressed in Section 6. Section 2 presents the complete flow structure and governing equations for planar motion, including the physical mechanisms listed earlier. The presence

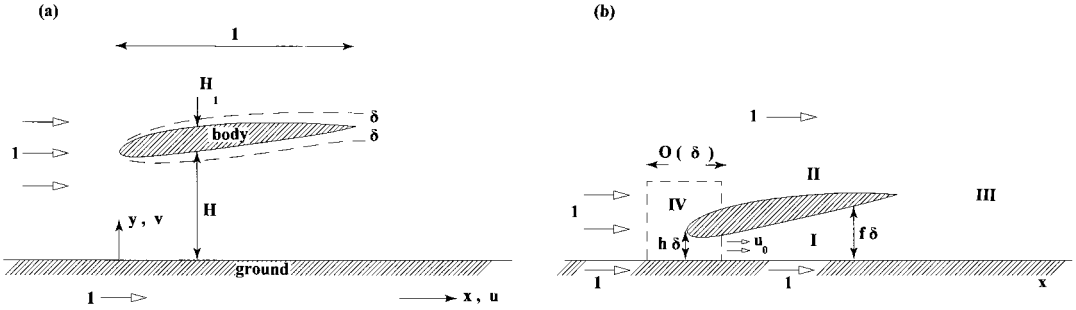

Figure 1. Flow structure and notation in body-ground interference, (a) for general H, H_1 with δ small, (b) for thin-gap thin-body configurations with $f, h \sim 1$ yielding regions I–IV. The coordinate origin is taken on the ground, at the foot of the arrow marked y, v.

of a streamwise jump discontinuity, in effect, at the leading edge is a particularly noteworthy feature from the standpoint of the overall flow past the vehicle body (and seems in line with the simulations and/or experiments in [2,3,8,21] and elsewhere, as does the viscous-inviscid balancing and downstream separated flow typical here). Computational methods are discussed in Section 3, followed by flow solution properties in Section 4. The latter shows numerical results for the induced surface pressure and shear stresses (surface shears, skin friction, skin drag), at the underbody surface and at the ground, along with streamline patterns, lift and drag, for various underbody shapes, some of which provoke separated motion . In addition properties of comparatively large or small gaps are investigated, in view of the numerical estimates in the preceding paragraph; related design features for a front-flap configuration are also addressed in an appendix. (Concerning a rear flap, the Gurney device consisting of a tiny fence standing normal to the rear flap surface for example is discussed in [22]). Section 5 then discusses edge effects. These are associated first with the wake, especially if there is flow reversal, and second with three-dimensional motion, which introduces yet more flow mechanisms, notably affecting the inflow and outflow conditions at the planform edges of the underbody. Further comments are made in Section 6, together with the account of the turbulent modelled case, for which the laminar two- and three-dimensional properties in sections 4,5 especially for comparatively large gaps prove directly relevant, and comparisons with recent experiments.

2. The flow structure

The working is expressed in nondimensional terms based on Cartesian coordinates (x, y) and corresponding velocity components (u, v) measured relative to the typical body length ℓ^* and body speed u^* respectively, together with nondimensional pressure variations p based on $\rho^* u^{*2}$ where ρ^* denotes the constant fluid density. Thus the body at height $y = H$ occupies the range of x between zero and unity in the frame moving with the body, while the ground is the x-axis, and the velocity (u, v) is to be zero on the body but $(1, 0)$ along the ground and in the farfield. The above, which is for a simple aligned flat plate body, generalises to other basic nondimensional body shapes of interest as in Figure 1(a), H then being the characteristic vertical gap width and H_1 the characteristic body thickness.

Three prime configurations of current relevance are the following, with δ denoting the small characteristic boundary layer thickness:

(i) H, H_1 comparable, each much greater than δ (thick gap, thick body);

(ii) H comparable with δ, but H_1 greater (thin gap, thick body);

(iii) H, H_1 both comparable with δ (thin gap, thin body).

The flow in configuration (i) is likely to be similar to that in external aerodynamics and tends to lead, with viscous forces present, to large-scale separation as if past a bluff body; see also [10] and later in this paragraph. Configuration (ii) is different from that, due to the closeness of the ground, although large-scale separation cannot be discounted as we shall see in the later discussion. Configuration (iii) is found to yield more confined flow separations, if any. Our focus in the present study settles initially on the case (iii) of a thin gap and thin body with near-alignment, but the work involved also covers the thin-gap thick-body case of (ii) if separation is not too large-scale then and the work even approaches the thick-gap thick-body case in (i) as H, H_1 are eventually increased. The research in fact is guided by the analytical and computational findings in [10]. The latter starts with a fourth case,

(iv) H of order unity, H_1 comparable with δ (thick gap, thin body)

of separation-free motion for an external thin airfoil, followed by study of the effects of decreasing H, where inviscid thin-gap theory applies. This then forces significant viscous-inviscid interaction to grow at the trailing edge, the interactive influence spreading out in the streamwise direction as H is reduced further. Indeed, the spread of viscous effects is such that when H is decreased to become comparable with δ, giving the configuration (iii) of the current study, viscous-inviscid interaction fills or nearly fills the entire gap flow, starting from the leading edge.

The dominant scales for the flow in (iii) are illustrated in Figure 1(b). In most places clearly x is of $O(1)$, comparable with the body length, y is $O(\delta)$ scaled on the gap and body widths, u is $O(1)$ because of the unit ground speed, v is $O(\delta)$ by the continuity balance, and p is of $O(1)$ from the momentum balance. Similarly, if the flow is unsteady then a nondimensional time scale of order unity is expected, based on the ground speed and the body length. The above orders of magnitude hold true for regions I–III of the motion, in the gap, above the body and in the wake ($x > 1$) in turn. There is also a distinct small region (IV), in the vicinity of the leading edge, wherein x is reduced to $O(\delta)$, comparable with the y scale, while v rises to $O(1)$, comparable with u, and this leading-edge region plays an important role. Other less significant regions of flow are also induced but are of no concern here.

In the flow regions I–III, then, the velocity and pressure take the form

$$(u, v, p) = (u, \tilde{v}\delta, p) + \dots, \text{ with } (x, y) = (x, \tilde{y}\delta). \tag{2.1}$$

The governing equations in the gap region I in particular are the two-dimensional viscous interactive-boundary-layer balances of continuity and streamwise momentum,

$$u = \frac{\partial \tilde{\psi}}{\partial \tilde{y}}, \quad \tilde{v} = -\frac{\partial \tilde{\psi}}{\partial x}, \tag{2.2a}$$

$$u\frac{\partial u}{\partial x}+\widetilde{v}\frac{\partial u}{\partial \widetilde{y}}=-\frac{dp}{dx}+\frac{\partial^2 u}{\partial \widetilde{y}^2}, \tag{2.2b}$$

with $\widetilde{\psi}$ being the scaled stream function (such that $\widetilde{\psi}$ is zero along the ground $\widetilde{y}=0$) and with $\partial p/\partial\widetilde{y}$ being zero from the normal momentum balance, leaving p dependent on x above. The boundary conditions are

$$u=1, \quad \widetilde{v}=0 \quad \text{at} \quad \widetilde{y}=0, \tag{2.3a}$$

$$u=\widetilde{v}=0 \quad \text{at} \quad \widetilde{y}=f(x), \tag{2.3b}$$

$$u=u_0 \quad \text{at} \quad x=0+, \tag{2.3c}$$

$$p(1)=0. \tag{2.3d}$$

The constraints (2.3a,b) are from the ground and (under)body conditions, the underbody lying at a prescribed height $f(x)\delta$ where $f(x)$ is positive for $0 \leqslant x \leqslant 1$, and $f(0)=h$ is of order unity, so that the leading-edge height defining H say is $h\delta$ here. The constraint (2.3c), which holds for all y between zero and h, with u_0 an unknown positive constant, is explained below, whereas (2.3d) is the pressure-match condition with the wake flow of region III. The pressure $p(x)$ in the gap I is unknown, making the viscous flow there interactive in the sense of having prescribed displacement, but the physical expectation is that overall p must fall with increasing x along the gap, at least if the gap width varies gently. On the other hand p is identically zero in both of regions II, III, owing to the match with the free-stream properties $u\equiv 1,\ p\equiv 0$ at large positive $\widetilde{y}$, and so (2.3d) is implied. Earlier derivations and study of (2.2),(2.3) are in [13,15,17].

The requirement (2.3d) is equivalent to the Kutta trailing-edge condition. It poses, at first sight, a dilemma because of the overall favourable pressure gradient along the gap noted above, suggesting a pressure mismatch at the leading edge. The resolution is provided by the small extra region IV which surrounds the leading edge and across which (streamwise) there has to be a pressure jump from zero upstream of the gap to an unknown constant p_0 just inside the gap. The flow properties of region IV, in which

$$(u, v, p)=(U, V, P)+\ldots \quad , \ (x, y)=(\widetilde{x}\delta, \widetilde{y}\delta), \tag{2.4}$$

are essentially inviscid, with the Euler equations applying to U, V, P as unknown functions of $\widetilde{x}, \widetilde{y}$. The vorticity is identically zero throughout region IV however as the incident flow upstream is the stream $u\equiv 1, v\equiv 0$, and so the local stream function Ψ (defined by $U=\partial\Psi/\partial\widetilde{y},\ V=-\partial\Psi/\partial\widetilde{x}$) satisfies Laplace's equation. The boundary conditions holding on Ψ require Ψ to be zero along $\widetilde{y}=0$, for tangential flow at the ground, Ψ to tend to $\widetilde{y}$ in the farfield outside the gap, and Ψ to be a constant Ψ_0, say, along the body shape at the leading edge, this shape being locally flat so that $\widetilde{y}=h$ in effect. This last is again for tangential flow, ruling out separation at the leading edge. The full solution for Ψ is shown in Appendix A. The main features of interest here follow from mass conservation, implying that $\Psi_0=hu_0$ since U tends to the constant u_0 at large positive $\widetilde{x}$ in the gap, and momentum conservation (Bernoulli). The latter yields $P+U^2/2$ being preserved at its input value of $\frac{1}{2}$ along all streamlines in region IV and hence the downstream pressure at the end of IV is given by $p_0+u_0^2/2=\frac{1}{2}$. Returning to the formulation for the interactive boundary layer region I, therefore, the starting condition (2.3c) is to be combined with

$$p(0+) = p_0 (= \tfrac{1}{2} - \tfrac{1}{2}u_0^2). \tag{2.5}$$

The starting-pressure constant p_0 which determines the u_0 value in (2.3c) is unknown and has to be guessed/modified in order for the end-pressure condition (2.3d) to be satisfied. Further, the value of the stream function $\widetilde{\psi}$ at the underbody is to remain at hu_0 throughout the gap I, consistent with (2.2a),(2.3c). The strong adjustment at the leading edge implicit in (2.3c) agrees with the leading-edge jump features found for internal branching flows in [23], and for nonsymmetric blade-wake interactions in [24], and all in a sense reflect the strength of the Kutta requirement at the trailing edge or further downstream.

The same boundary-layer equations (2.2a,b) apply for regions II, III but with

$$p(x) \equiv 0 \quad \text{(in II, III)}, \tag{2.6}$$

from the free-stream matching mentioned previously. This indicates non-interactive flows in II, III at first glance. The flow in region II above the body starts with the uniform stream $u = 1$ at $x = 0+$, for all $\widetilde{y}$ greater than h, followed by the no-slip constraint at $\widetilde{y} = g(x)$ and $u \to 1$ at large positive $\widetilde{y}$, for $0 < x < 1$. Here $g(x)\delta$ specifies the upperbody surface, satisfying $g(0) = h$ $(= f(0))$ at its leading edge and $g(1) = f(1)$ for body closure at the trailing edge. Hence, from a Prandtl transposition, the Blasius solution describes the region II flow in coordinates x, $\widetilde{y} - g(x)$. That solution also specifies the upper part $(\widetilde{y} > f(1))$ of the starting velocity profile for the wake region III at $x = 1+$, the lower part $(0 \leqslant \widetilde{y} < f(1))$ being specified by the velocity profile of region I at $x = 1$. Thus determining the flow in III depends on determining the flow in I first, at least in the absence of significant flow reversal.

The central task is the interactive one of solving (2.2a,b),(2.3a–d),(2.5) for the nonlinear motion in the gap I. This is addressed in the next two sections under various conditions, including separated flow properties. Meanwhile we remark on the physical mechanisms active here. They involve the viscous forces coupling with the inviscid effects across the entire gap; the quasi-fixed displacement helping to drive the viscous gap boundary layer and determine its pressure variation; the trailing-edge constraint; the pronounced upstream influence; the associated jump conditions at the leading edge; and the influence of the moving surface (ground) driving forward x-flow near the ground. The quasi-fixed displacement above allows separation in the sense of reversed flow to be incorporated regularly in the flow description. Moreover, the leading-edge jumps in (2.3c),(2.5) can occur because of the presence of solid containing surfaces (here one fixed, one moving) to withstand the substantial local pressures generated, and likewise in internal branching flows [23], whereas in the blade-wake interactions [24] also noted earlier the surrounding shearing motions are able to act instead to absorb the abrupt pressure rise or fall locally.

3. Computational methods

Two numerical methods were used to solve (2.2a,b),(2.3a–d),(2.5) computationally for the gap flow I and were checked against each other. They are based on finite differences and are outlined in the next two paragraphs. The computational task has to incorporate upstream influence through the unknown starting pressure p_0 as discussed in Section 2 and this was treated by streamwise iteration, multi-sweeping in x to find that p_0 value which leads to satisfaction of the zero $p(1)$ requirement. An alternative was considered, of setting p_0, marching downstream just once until the pressure p reaches zero and then renormalising the lengths and velocities appropriately, but that leads to uncontrolled grids and in any case the present

approach proved relatively inexpensive in computing time. Further, close to the starting point of region I for x small and positive the flow solution near each solid surface is Blasius-like, in the sense that the similarity equation

$$S''' + \tfrac{1}{2} S S'' = 0 \tag{3.1}$$

holds there for the scaled effective stream function $S(\eta)$. Several previous works, including [17], have discussed the nature of the singularity at $x = 0$. Near the ground $\widetilde{y} = x^{1/2}\eta$ is small, $\widetilde{\psi} \sim x^{1/2} S$ and the boundary conditions relevant are $S(0) = 0,\ S'(0) = 1,\ S'(\infty) = u_0$, whereas near the underbody $\widetilde{y} - h = -x^{1/2}\eta$ is small, $\widetilde{\psi} - h u_0 \sim -x^{1/2} S$, and S satisfies $S(0) = S'(0) = 0,\ S'(\infty) = u_0$. In between, for $\widetilde{y}$ of order unity between zero and h, there is an inviscid core with a small $O(x^{1/2})$ perturbation of $u = u_0,\ \widetilde{\psi} = y u_0$ and from the mass and momentum balance (2.2a,b) the induced pressure $p - p_0$ is $O(x^{1/2})$. These irregular starting behaviours provide guidelines on the fine mesh distribution required computationally.

The first numerical method accommodates the above three-tiered starting behaviour directly, and it proceeds as follows, assuming for now that there is no flow reversal, so that u is non-negative. The two Blasius-like solutions and the core solution are set at the first downstream computational station. Then forward marching is conducted in x, using a three-point backward differencing in the streamwise direction and three-point centred normally, together with grid stretching to allow for rapid solution responses near the leading and trailing edges for example. A secant scheme was employed to deal with the end condition (2.3) iteratively. If flow reversal (negative u) is encountered, the above is modified by use of the well-known Flare approximation, *i.e.* neglecting the term $u \partial u / \partial x$, in the first forward sweep and then windward differencing in subsequent sweeps (see also Sections 4, 5.1). The typical grids used had steps of approximately 10^{-3}, $10^{-3} - 10^{-4}$ in $x, \widetilde{y}$, respectively, and the nominal accuracy of the present results was confirmed by re-computing on different grids.

The second method is a semi-implicit procedure very similar to those used by [25,26] to cope with multiple successive leading-edge irregularities. It uses refined meshes rather than incorporating directly the three-tiered starting behaviour described near (3.1), it is stable, robust, simpler to program and adjust, and its accuracy is high with suitably refined grids. It proves equally inexpensive even though grid steps much smaller than in the first method are necessary for accuracy. The results from the two methods are virtually identical.

A third method is to adopt a multi-tier gridding approach, extending that of [27], to accommodate the three-tiered behaviour described near (3.1). This requires differencing in η instead of $\widetilde{y}$, near each surface tier, and coupling the solution numerically via a $\widetilde{y}$-differencing form in the core tier. The method has been developed in the current research programme but it proved cumbersome compared with the two methods described earlier.

A similar approach applies in the wake region III except that there p is set to zero and instead the boundary-layer displacement is to be found. So the flow problem there is more of the classical-boundary-layer type (see also Sections 4, 5.1), while the classical Blasius boundary layer accounts for region II.

The results presented below are all obtained using the first computational method.

4. Flow properties

Pressure, surface shear, streamlines, velocity profiles, separation. Computational results for region I are shown in Figures 2–5. Figure 2(a–c) presents the solutions for the pressure p,

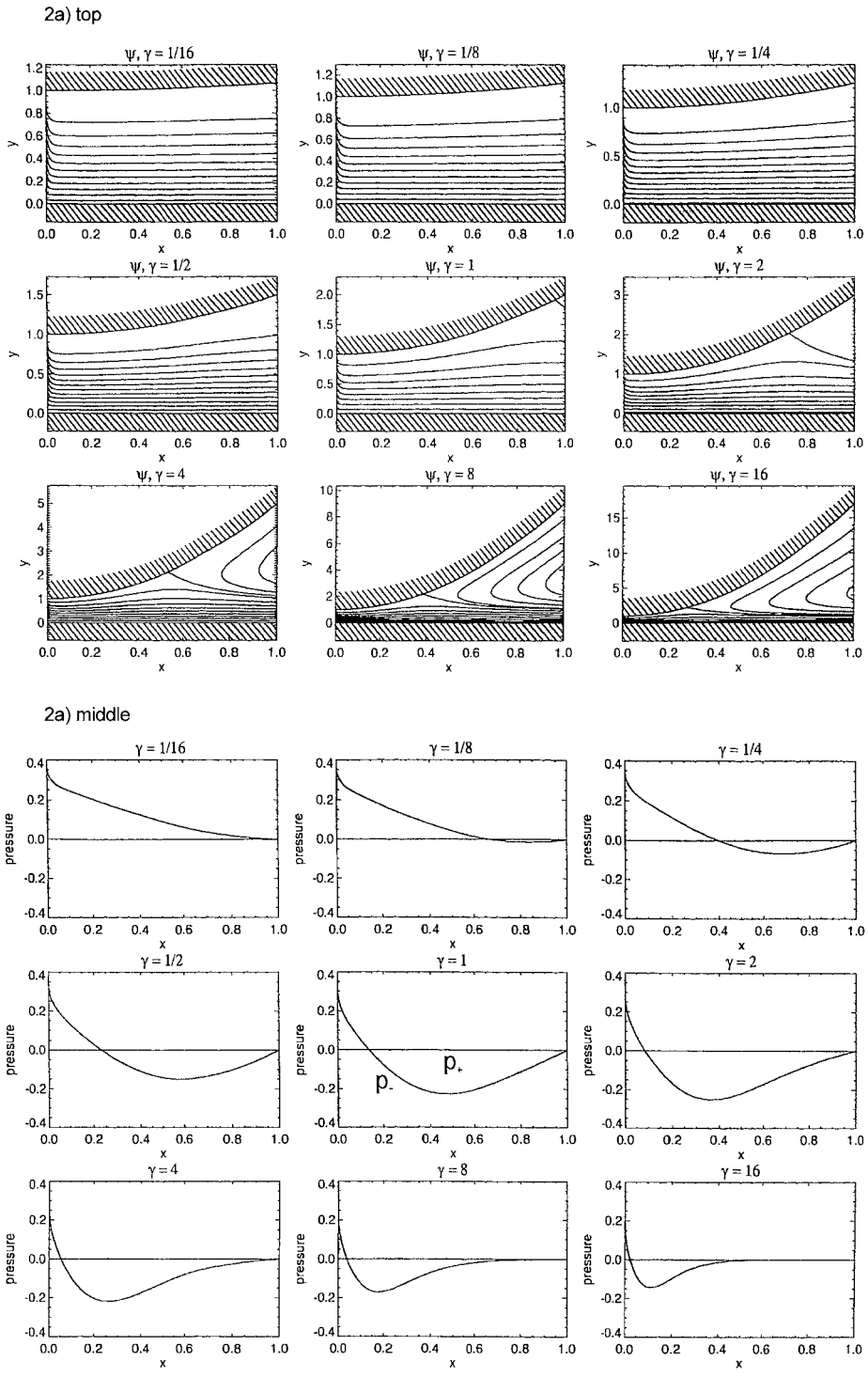

Figure 2. Computed gap-flow results for normalized streamlines, pressure and surface shears. (a) for $f(x) = h + \gamma x^2$, with $h = 1$ but $\gamma = \frac{1}{16}, \frac{1}{8}, \frac{1}{4}, \frac{1}{2}, 1, 2, 4, 8, 16$. (b) As (a) but $\gamma = 1$, with $h = \frac{1}{4}, 1, 4$.

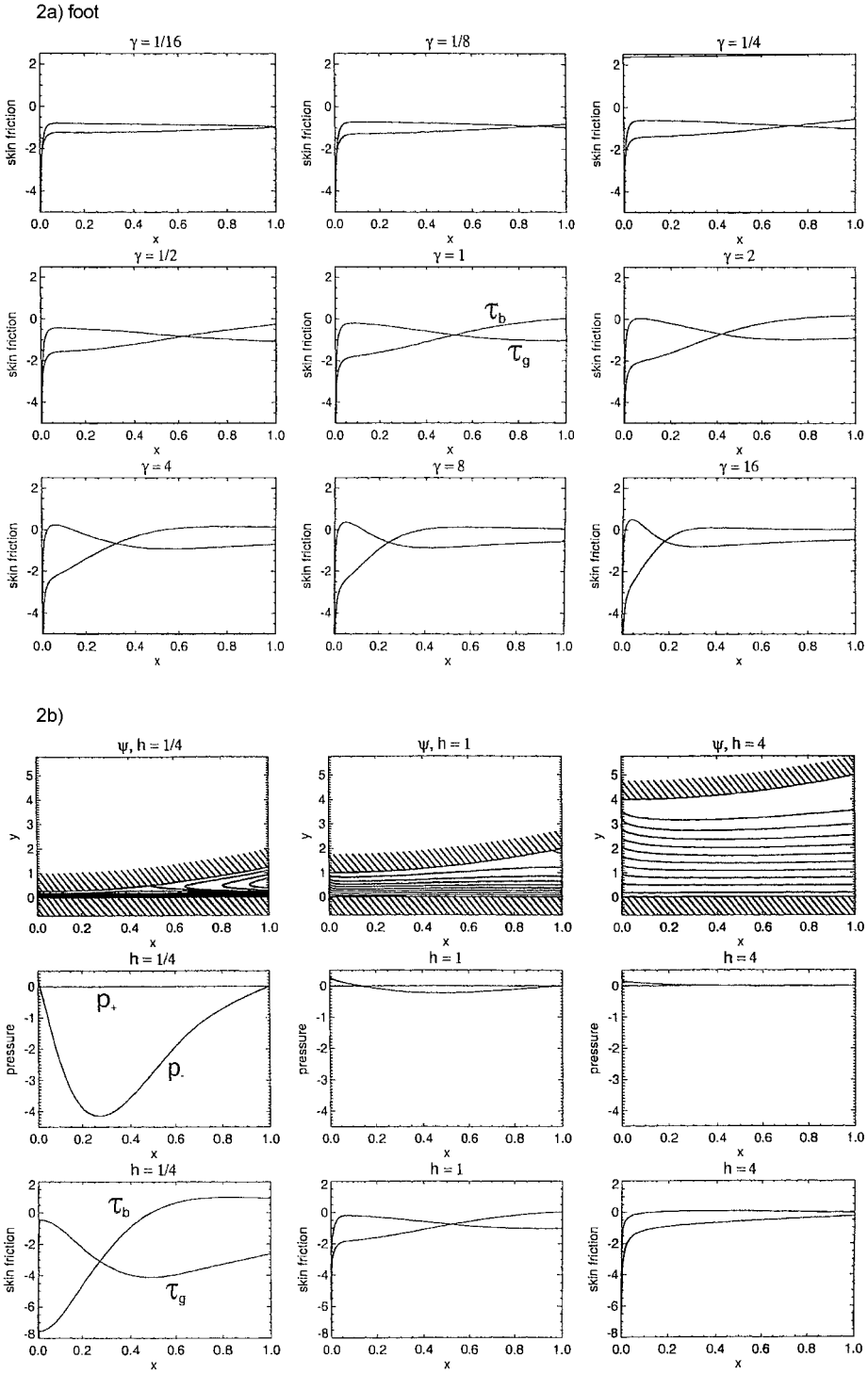

Figure 2. Continued.

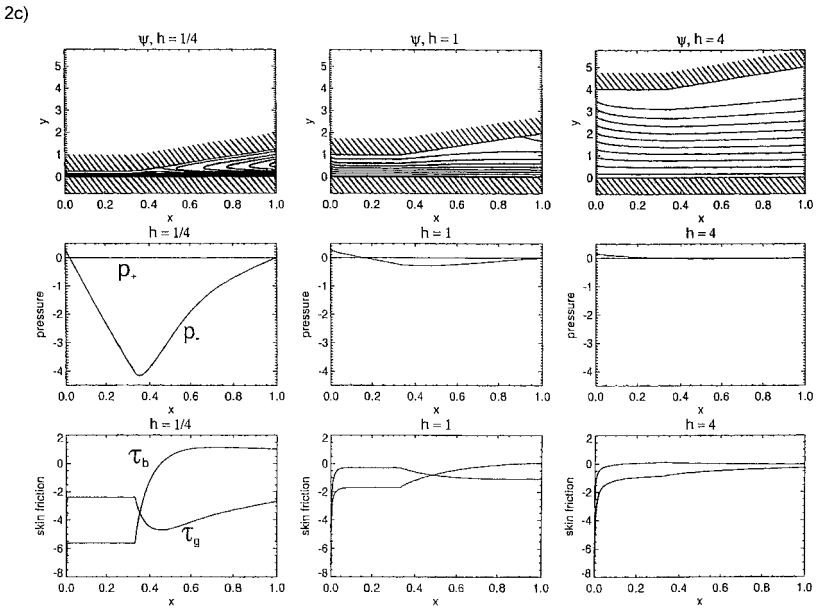

Figure 2. (c) For straight-line geometry shown, with junction at $x = \frac{1}{2}$, and $h = \frac{1}{4}, 1, 4$ (compare (b)).

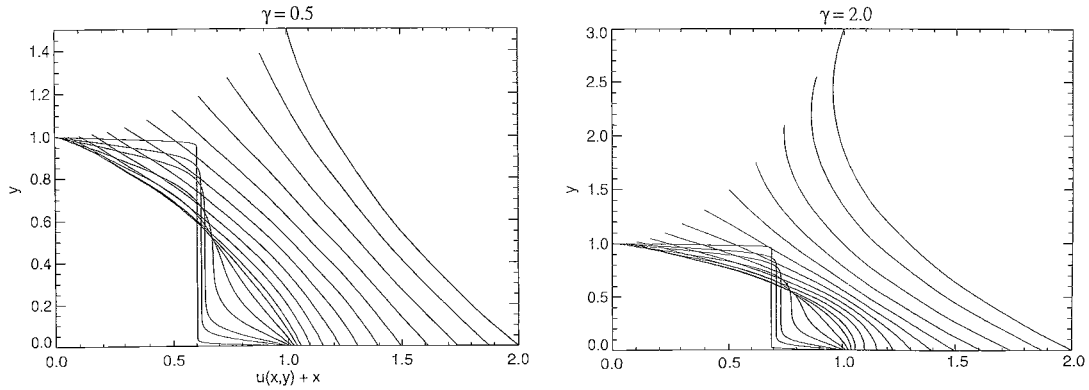

Figure 3. Velocity profiles in the gap for shapes of Figure 2(a) when $\gamma = \frac{1}{2}$ (all forward), 2 (partly reversed); $\tilde{y}$ is plotted against $u + x$.

the normalised surface shears τ_g (at the ground), τ_b (at the underbody) and the streamlines of constant $\widetilde{\psi}$, mostly for underbody shapes $f(x)$ given by $h + \gamma x^2$and a range of values of the gap width parameter h and the underbody curvature parameter γ. (The same shapes are used in Figures 3, 4). Here τ_g is defined as $\partial u/\partial \widetilde{y}$ at $\widetilde{y} = 0$ and τ_b as $\partial u/\partial \widetilde{y}$ at $\widetilde{y} = f(x)$. So the flow is forward in x near the underbody if τ_b is negative, but reversed if τ_b is positive, while near the ground any positive τ_g values correspond to an overshooting velocity profile, in the present moving frame. In more detail, Figure 2(a) shows in turn the streamlines, p and τ_b, τ_g for γ ranging from 1/16 to 16; Figure 2(b) shows the same properties but for fixed γ, with h between $\frac{1}{4}$ and 4; and Figure 2(c) is as 2(b) but with a straight-line geometry. Sample velocity profiles are given in Figure 3.

In most cases examined, *e.g.* that of $\gamma = \frac{1}{2}$ in Figure 3, the value of u_0 was found to remain between zero and unity, associated with fluid slowing down (across the leading-edge jump)

relative to the ground velocity. This is in line with the initial pressure p_0 being positive and hence an overall pressure drop along the gap region I, despite the many substantial regions of negative pressure seen in the results.

In some cases (*e.g.* $\gamma = 2$ in Figure 3), particularly with a pronounced expansion of the gap downstream, reversed flow (separation) is encountered, always signalled by τ_b becoming positive. The numerical results from windward differencing and from the Flare approximation were usually close together. In such flows the pressure p reaches a minimum, followed by an adverse pressure gradient leading to separation, which occurs with the flow solution remaining regular. If the separation is extensive there is then generally a relief of the pressure gradient, hinting at the approach to a pressure plateau, as the reversed motion is then comparatively slow. In fact, a sufficiently large extent of separation here (prior to any wake, as for example with rapid variations in underbody shape near the leading edge) causes a trend towards the majority of the momentum staying close to the ground, akin to breakaway separation in external aerodynamics. The viscous ground layer which is jet-like then has a characteristic $\widetilde{y}$-scale proportional to $x^{1/2}$, since the u-scale is of order unity of course, and the pressure gradient $p'(x)$ is negligible, so that a similarity form ensues of Blasius-like quality governed by (3.1) again but now with $S(0) = 0,\ S'(0) = 1,\ S'(\infty) = 0$. This yields $S(\infty)$ finite and positive. Above the ground layer a small uniform reversed velocity profile is expected, suggesting that $\widetilde{\psi}$ is $S(\infty)x^{1/2}$ times $[1 - \widetilde{y}/f_d(x)]$ provided the downstream form $f_d(x)$ of the underbody shape $f(x)$ is greater than $O(x^{1/2})$. Hence u is approximately $- S(\infty)x^{1/2}/f_d(x)$, which is small and negative as assumed and leaves the predicted pressure response as

$$p(x) \sim \text{constant} - \frac{S^2(\infty)x}{2f_d^2(x)}. \tag{4.1}$$

The plateau trend (4.1) is in keeping with the computed results.

Overshoot. In cases such as $\gamma = 4, 8, 16$ in Figure 2(a), where the pressure gradient produced is sufficiently favourable, τ_g is found to become positive and so indicates an overshoot in the velocity profile near the ground. In a frame fixed in the ground, *e.g.* for a stationary spectator, the local fluid motion is therefore temporarily in the opposite direction (rightwards) from that of the (leftwards moving) body, which is an interesting facet of such cases.

Lift and drag. The lift and drag responses are presented in Figure 4, the cases shown there corresponding to those of Figure 2(a–c) respectively. The lift is evaluated from integration of the pressure (p) over x, in the gap region I, given that p is zero above the body in region II. The lift contribution from the front part of the underbody is generally positive, in line with p_0 usually being positive there. Changes of sign can occur further downstream, however, to yield downforce, *i.e.*, negative lift. The drag is evaluated from integration over x of the scaled stress τ_b for skin drag added to that of $pf'\delta$ for form drag and is always positive. On the other hand the drag gradually decreases as the scaled curvature γ is increased, because of the ensuing reduction in skin drag then. The effects of flow separation on lift and drag are interesting, as Figure 5 shows. The figure concerns a front-flap (or forewing) shape that is horizontal for a distance ℓ from the leading edge and then straight but inclined, yielding an expansion ratio $f(1)/f(0)$ which is denoted by r. The design of this shape in order to produce the maximum downforce is considered in appendix B for order-one or small values of h and in more detail by [10].

Large h. The extremes of large h and small h are noteworthy, especially the former in view of the numerical estimates made in the introduction, and both extremes also prove to be relevant to the turbulent case studied in Section 6. (Analysis of these extremes in [17] was

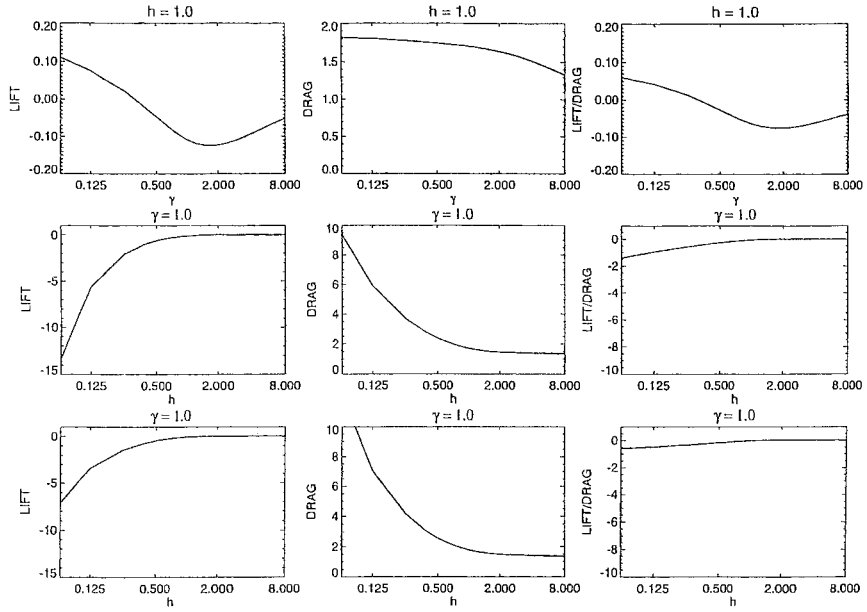

Figure 4. Lift, drag and lift/drag plotted against γ, for case of Figure 2(a), and against h, for cases of figs. 2(b), 2(c). The lift and drag are nondimensionalized with respect to the vehicle (or undertray) speed and streamwise length.

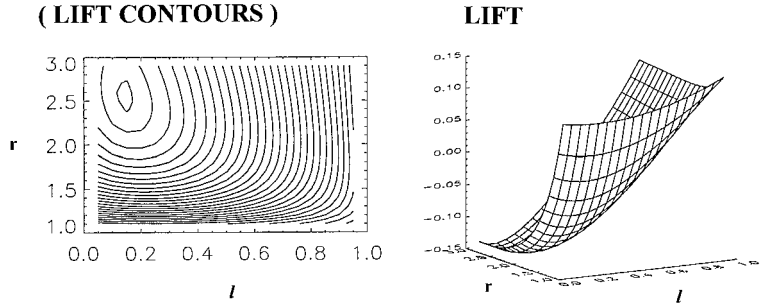

Figure 5. Lift L plotted against ℓ (the junction position) and r (the expansion ratio $f(1)/f(0)$), seeking maximum downforce, for straight-line geometry $f(x) = h$ in $0 \leqslant x \leqslant \ell$, $f(x) = h + (r-1)h\,(x-\ell)/(1-\ell)$ in $\ell \leqslant x \leqslant 1$. Here $h = 1$, while ℓ lies between 0, 1 and r between 1, 3. The left and right diagrams give different views of the trough in L. See Section 4 and, for fuller detail, Appendix B.

kindly pointed out to us by a referee.) For large typical h values and large f everywhere, the solution of (2.2a,b) is largely inviscid as long as there is no separation (see end of this paragraph), and so vorticity conservation implies that u depends only on x. Therefore $\widetilde{\psi}$ is $u(x)\tilde{y}$ from (2.2a),(2.3a). Mass conservation via (2.3b) then requires uf to remain equal to $u_0 h$ for all x, yielding $u(x) = u_0 h/f(x)$. Hence the momentum balance (2.2b) together with the end conditions (2.3d),(2.5) yields the solution

$$p = \tfrac{1}{2} - \frac{u_0^2 h^2}{2f^2(x)}, \quad \text{with } u_0 = \frac{f(1)}{h}, \tag{4.2a,b}$$

according to this thin-gap theory which assumes attached viscous boundary layers. The form (4.2a,b) is also derived in [17]. For a near-uniform underbody shape $f = h + f_1(x)$, as one example, with f_1 small compared with h, the value of u_0 is thus $1 + h^{-1} f_1(1)$ and so the

pressure produced becomes $p = (f_1(x) - f_1(1))/h$. This pressure is positive or negative ($p_0 = -f_1(1)/h$) near the leading edge (depending on whether the gap contracts or expands), zero at the trailing edge, and scales inversely with h, as noted earlier: see also [23]. The computational results (Figure 2) tend towards these analytical ones as h increases. In some cases separation still occurs and then f should be replaced by f-effective (body shape plus eddy shape), where [23] shows f-effective to be virtually uniform (a horizontal eddy boundary) from the separation point onwards. This not only reinforces the point made in section 1 about substantial boundary layer thickening but also agrees with the trend of the computational results of Figures 2,3.

Small h. For small typical h, f, most of the gap flow is governed by the lubrication forces of pressure gradient and viscous diffusion and so u is $p'\tilde{y}^2/2 + \tau_g\tilde{y} + 1$, whereupon (2.3a,b) lead to two equations for p', τ_g , giving

$$p' = 6f^{-3}(f - 2hu_0), \quad \tau_g = -f^{-1}(1 + p'f^2/2). \tag{4.3a,b}$$

This assumes h^2u_0 to be small, for typical x of order unity, and we notice that $|p|$ is large of order h^{-2} usually depending on the unknown u_0. (Again, the form (4.3a,b) is also derived in [17]). For the special case of a straight underbody, $f = h$ for all x and hence $p(x)$ is $6h^{-2}(1 - 2u_0)(x - 1)$ on use of (2.3d); then guessing that $p(0+)$ is necessarily zero on this length scale predicts $u_0 = \frac{1}{2}$ (hence p is identically zero on the h^{-2} scale), as in Couette flow under zero pressure gradient with $\tau_g = -1/h$. The computations do indeed show u_0 approaching $\frac{1}{2}$, in agreement with the prediction. For general non-straight underbodies, where integration of (4.3a) with (2.3d) is required, similarly we expect $p(0+)$ to be zero on this scale (fixing u_0) since the characteristic pressure variation here is much greater than that near the leading edge. The latter, at a short x scale of order h^2, has the inertial forces reasserting themselves, with $(x, \tilde{y}, u, \tilde{v}, p, \tilde{\psi})$ normalised on

$$(h^2, h, 1, h^{-1}, 1, h), \tag{4.4}$$

which keeps (2.2a,b) intact. No substantial overshoots arise in the velocity profiles. The local problem for (4.4) is the same as in Section 2 except that h, f are both replaced by unity and the normalised x continues to downstream infinity, implying that p generally decreases linearly at large x. (A substantial underbody shaping f near the leading edge, on the h^{-2} length scale, can lead instead to the separated-flow result (4.1).) The unknown constant p_0 has to be fixed such that $u_0(\equiv (1 - 2p_0)^{1/2})$ supplies the exact mass flux hu_0 (across the gap) required by the subsequent lubrication balance downstream, along with (2.3d). The typical $|p|$ near the leading edge is usually only 0(1), however, and we take it to be much less than $O(h^{-2})$; see (4.4). Hence the $p(0+)$ condition applies as described above, on the scale x of order unity, which then determines u_0. Again the computational results are in line with this behaviour.

The lift for large values of h is of order unity for the general underbody shape in (4.2a,b), but small for the near-uniform shape involving f_1. The corresponding pressures are $O(1)$ or scale with h^{-1}. For small h, on the other hand, the lift is generally large, of order h^{-2} from (4.3a), as is the pressure, although for the straight underbody shape for instance the lift is small of order h^2 because of the order-one pressure variation in (4.4). For that special case of a straight underbody shape the lift stems in fact from the viscous-inviscid boundary-layer contribution, whether h is large or small.

5. Edge effects: wakes and three-dimensional flows

The effects of the trailing and/or side edges become significant when wakes and/or three-dimensional motions are considered, in Sections 5.1, 5.2 respectively.

5.1. THE WAKE

The planar-flow computations of the previous two sections were continued beyond the trailing edge into the wake III, wherein p is identically zero. The flow solution in III is clearly affected by the velocity profiles entering from regions I,II. Indeed just beyond the trailing edge, at small positive $x-1$, a Goldstein-like similarity form holds near $\tilde{y} = f(1)$, with $\tilde{\psi} \sim (x-1)^{2/3}T(\tilde{\eta})$ satisfying

$$T''' + \tfrac{2}{3}TT'' - \tfrac{1}{3}T'^2 = 0 \tag{5.1}$$

subject to $T' \sim \pm\lambda_{\pm}\tilde{\eta}$ as $\tilde{\eta} \to \pm\infty$. Here $\tilde{y} - f(1) = (x-1)^{1/3}\tilde{\eta}$, the positive constant λ_+ is the Blasius wall shear from II, and λ_- is the underbody shear $-\tau_b(x=1)$ from I. The solution of (5.1) requires λ_- to also be positive in general. The requirement is quite consistent with totally forward flow (relative to the body) in the gap I, but if the gap flow contains some flow reversal (relative to the body) near the underbody, in the interval $0 < x < 1$, then there has to be a reattachment prior to the trailing edge in order to make λ_- positive. See the explanation of trailing-edge separations in [29]. This requires extra care in the computations with reversed motion, as it reflects a back-effect of the flow in the wake III on that in the gap I, among other effects.

Results for the wake are presented in Figure 6(a,b) for the straight-line body shapes shown. Without flow reversal (2.2a,b) can be marched forward readily downstream from the trailing edge at $x = 1$, with (2.6). The motion shows gradual diffusion downstream to the uniform stream, with the velocity profiles relaxing as in the figure. With flow reversal the wake III computations proved far more difficult. Concerning the back-effect of the preceding paragraph, previous results in the gap I are in fact hardly affected by the choice of Flare or windward differencing, but the latter is crucial to III, as is the use of very refined grids. Most success was achieved with the stream condition $u = 1$ and a mass-flux constraint imposed at a finite value $y = y_\infty$ (as if for a remote wind-tunnel wall, say) and hence nonzero unknown pressure p. In the limit of y_∞ large the pressure p tends to zero in line with (2.6). Separated flow results are included in Figure 6(a,b); in each of the diagrams of scaled shear in Figure 6(a) note that the above-body values τ_{b^+} are given by the uppermost curve while the ground values τ_g are given by the curve that extends the furthest to the right. The separated flow results bear some resemblance to the trailing-edge separations mentioned above but three extra facets stand out. One is the existence of a second, relatively small, eddy close to the trailing edge, with a corresponding streamline pattern which is rather intricate as the flow adjusts to produce non-negative shear λ_- at the trailing edge. The second facet is the comparatively short streamwise scale of the closure of both eddies. We note a possibility raised by Dr. S.N. Timoshin of a square-root singularity at closure within III, given (2.6). It may be that, as $y_\infty \to \infty$ and $p \to 0$, the closure positions x actually both tend to unity. If so this points to the presence of a distinct abrupt jump region near the trailing edge between regions I,III similar to that (IV) near the leading edge. Again, Dr. J.R.Ockendon raised the double jump possibility from a different viewpoint. It would be interesting to pursue the present separated wake issue further [10], and we observe also the analogy with the inflow and outflow conditions described in

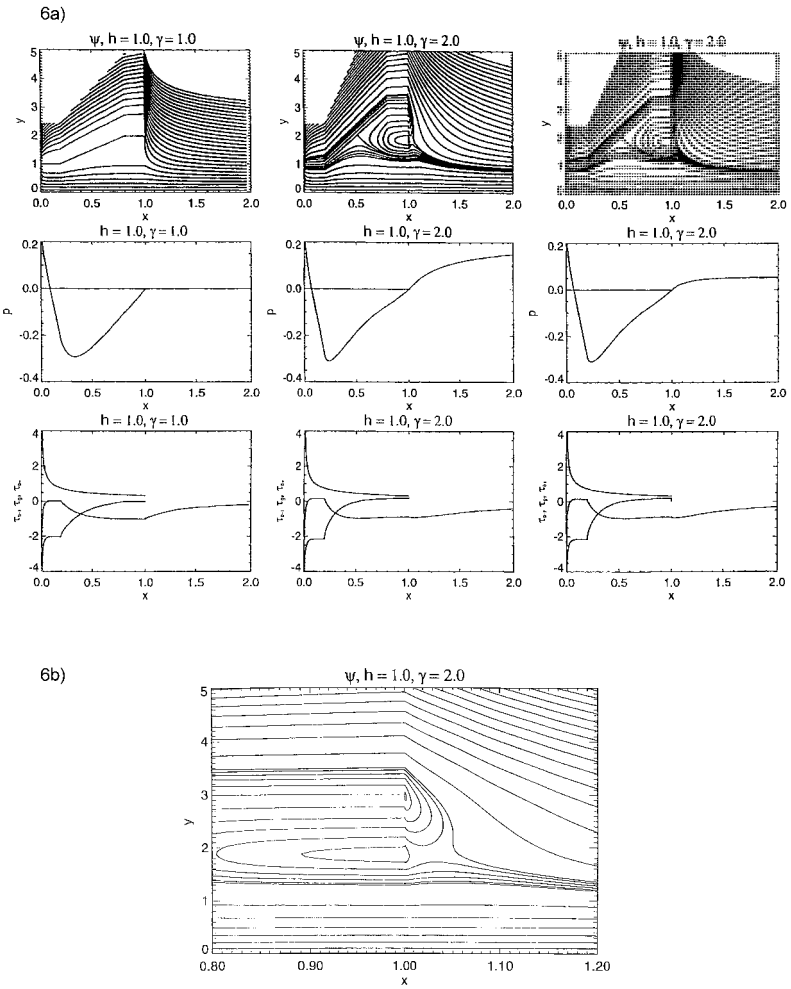

Figure 6. Wake results showing streamlines, pressures and wall shears, for forward and separated flows; see Section 5.1. In the middle and right-hand results, extra streamlines are plotted within the reversed flow to show details there, and $y_\infty \approx 32$, while ψ values at $y = y_\infty$ are constant and constant $+1{\cdot}5(x-1)^{1/3}$ respectively. Notice the reduced wake pressure variation in the right-hand case.

the next sub-section. The third facet is that fluid is drawn down from the above-body surface, apparently, into the reversed flow in the gap below the underbody, to entirely fill the separation there.

5.2. THREE-DIMENSIONALITY

In the three-dimensional extension of the work, the flow structure of Section 2 remains intact although several new issues arise. Regions I–III have the spanwise coordinate z and corresponding velocity w of order one and the three-dimensional governing equations

$$\frac{\partial u}{\partial x} + \frac{\partial \tilde{v}}{\partial \tilde{y}} + \frac{\partial w}{\partial z} = 0, \tag{5.2a}$$

$$u\frac{\partial u}{\partial x} + \tilde{v}\frac{\partial u}{\partial \tilde{y}} + w\frac{\partial u}{\partial z} = -\frac{\partial p}{\partial x}(x, z) + \frac{\partial^2 u}{\partial \tilde{y}^2}, \tag{5.2b}$$

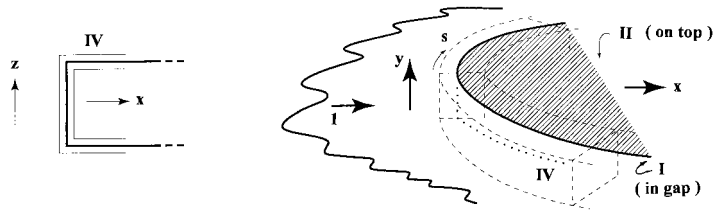

Figure 7. Sketch of the three-dimensional flow structure, in particular indicating the thin region IV wherever inflow exists into the gap I for straight or curved edges $k(x)$ of the planform. In the right hand diagram the dots correspond to the exact position of the leading edge $z = k(x)$ and the dashes to the thin leading edge region, while the wavy line indicates the extensive ground.

$$u\frac{\partial w}{\partial x} + \tilde{v}\frac{\partial w}{\partial \tilde{y}} + w\frac{\partial w}{\partial z} = -\frac{\partial p}{\partial z}(x, z) + \frac{\partial^2 w}{\partial \tilde{y}^2}, \tag{5.2c}$$

cf. (2.2a,b), while the boundary conditions in the gap I are analogous with (2.3a–d),(2.5), such that

$$u = 1, \quad \tilde{v} = w = 0 \quad \text{at} \quad \tilde{y} = 0, \tag{5.3a}$$

$$u = \tilde{v} = w = 0 \quad \text{at} \quad \tilde{y} = f(x, z), \tag{5.3b}$$

unknown inlet conditions at leading edges, (5.3c)

exit pressure $p = 0$ at trailing edges. (5.3d)

Similar constraints to those in Section 2 hold in the outside regions II, III. In (5.2b,c) the pressure $p(x, z)$ is unknown, independent of $\tilde{y}$. In (5.3b) f signifies the three-dimensional underbody shape. The conditions (5.3c,d) reflect, respectively, the existence of a leading-edge jump across the analogue of region IV, which (being comparatively thin) can be assumed to be quasi-planar, and the trailing-edge pressure match, since in regions II, III p is identically zero within the current flow structure. See Figure 7. The so-called leading edges are equivalent to positions of inflow into the gap I and the trailing edges to outflow. The side boundary conditions can be troublesome for a rectangular shape f with side edges aligned with the car motion, say; but the general approach, of designating (each part of) every edge as a leading or trailing edge depending on inflow or outflow, shows the way forward. This is so even when, as in the rectangular case above and in many nonlinear cases, the presence of inflow or outflow along an aligned edge is not known in advance, 'designating' then meaning 'guessing'. This aspect regarding inflow and outflow is a further (three-dimensional) flow mechanism, on top of the leading-edge jump mechanism.

Concerning (5.3c) in more detail, at a general curved inflow edge or part of it, if in planform β is the angle between the tangent to the edge and the outer stream direction (x-axis), then the constraint reads

$$u\cos\beta + w\sin\beta = \cos\beta \quad \text{(at inflow edges)}. \tag{5.4}$$

Here $\tan\beta = \mathrm{d}k/\mathrm{d}x$ if the edge is given by $z = k(x)$. The constraint (5.4) stems from the thin region IV lying along the inflow edge as in Figure 7. In IV the horizontal velocity component normal to the edge adjusts in a quasi-planar manner along with v as in Section 2 (compare

(2.4)), the distance coordinate s along the edge being of order unity, but the tangential component is convected pressure-free along the inward directed streamlines locally. Consequently the horizontal velocity tangential to this edge is continuous across region IV, as reflected in (5.4) (which resembles a condition across an oblique shock in compressible fluid flow). In (5.4), furthermore, u, w are expected to be independent of $\tilde{y}$, although usually they depend on s. For two-dimensional flows, as a check, β is $\pi/2$, w is zero and so (5.4) is satisfied identically and becomes redundant, in keeping with the constant in (2.3c) being an unknown. For aligned edges, β is zero, so that (5.4) becomes $u = 1$, this tangential velocity then being continuous as long as there is inflow. For the general case, however, (5.4) replaces (5.3c) at all the quasi-leading edges, whether they are known or unknown in advance.

A still further three-dimensional mechanism is also observed to be active. The mechanism concerns the extra upstream influence associated with the interactive boundary layer (5.2a–c) with fixed displacement but in three dimensions and is related loosely to Squire's theorem, as explained in [30]. This is additional to the influence of the unknown starting pressure (or u, w uniform inlet velocity) in (5.4) at each inflow boundary, and it increases the complexity of the computational task [29,31]. Moreover, the overall flow structure is without any influence from the motion outside the gap on the motion inside. This raises the interesting issue of whether the length and velocity scales of the gap I also hold outside in regions II, III, and whether there is no stronger and more concentrated vortex roll-up outside (as from the edges of a delta wing). The closeness of the body to the ground and (hence) the relatively thick boundary layers (if any) flowing out of the gap I should help prevent such roll-up occurring.

For large h, which we recall tends to be the most realistic range, the inviscid version of (5.2a)–(5.3d) indicates that u, w can be independent of $\tilde{y}$ throughout the gap. Then $\tilde{v} = -\tilde{y}(\partial u/\partial x + \partial w/\partial z)$ from (5.2a), (5.3a) essentially, and tangential motion at the underbody implies that $\partial(uf)/\partial x + \partial(wf)/\partial z$ is zero, which, coupled with the inviscid momentum balances, yields three equations for u, w, p as functions of x, z. This is for separation-free inviscid thin-gap flow. Assuming those momentum balances lead to the vertical vorticity being zero, we have $\partial w/\partial x$, $\partial u/\partial z$ both equal to $\partial^2\phi/\partial x\partial z$ say and so the single governing equation

$$\frac{\partial}{\partial x}\left(f\frac{\partial\phi}{\partial x}\right) + \frac{\partial}{\partial z}\left(f\frac{\partial\phi}{\partial z}\right) = 0 \tag{5.5}$$

holds for the vertical quasi-potential $\phi(x, z)$.The corresponding pressure p is given by $(1 - \phi_x^2 - \phi_z^2)/2$ throughout, and hence at outflow boundaries (5.3d) leads to the constraint

$$\left(\frac{\partial\phi}{\partial x}\right)^2 + \left(\frac{\partial\phi}{\partial z}\right)^2 = 1 \text{ (at outflow edges)}, \tag{5.6a}$$

whereas at inflow boundaries p, u, w are unknown functions of the distance s. The inflow constraints are

$$\phi = x \quad \text{at all } z = k(x) \text{ (inflow edges)} \tag{5.6b}$$

from (5.4), after integration with ϕ set to zero at $x = 0$. A solution is presented in Figure 8(a) for a rectangular planform of sides 1, $B(= \frac{1}{2})$ in x,z respectively with an oncoming wind at incidence. The elliptic boundary conditions necessary here with (5.5), which is close to Laplace's equation, verify the extra upstream influence in three dimensions mentioned in the previous paragraph. Indeed for near-uniform underbody shapes where $f = h + f_2$, $\phi =$

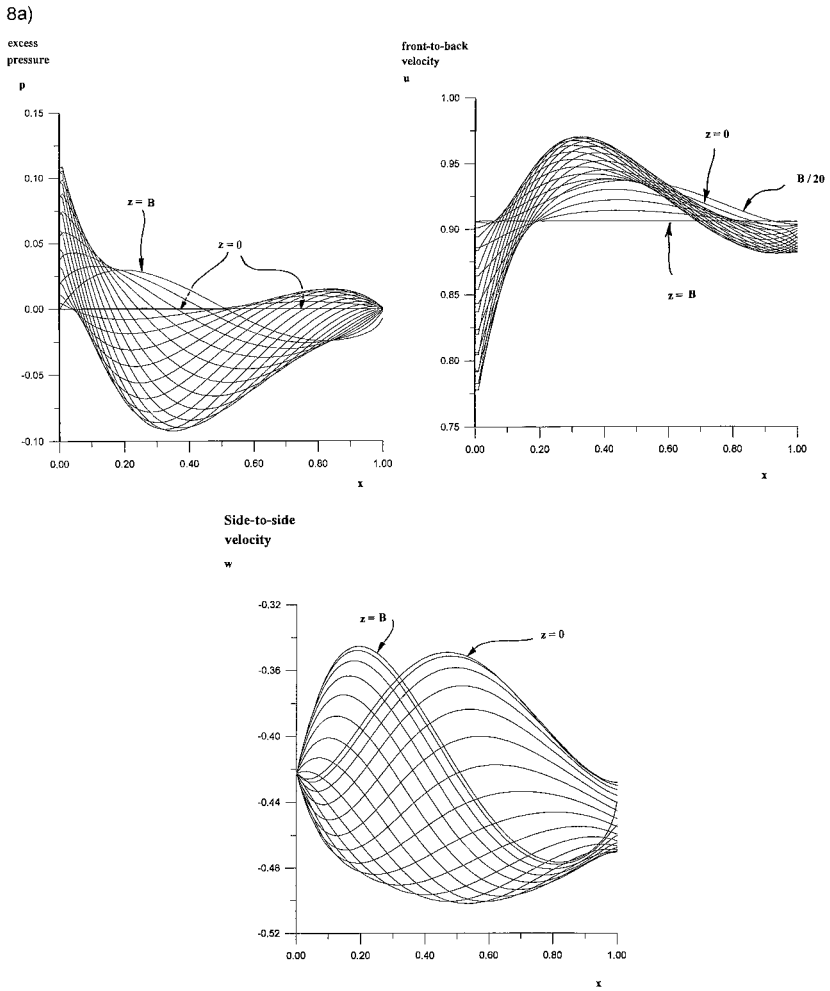

Figure 8. Computed three-dimensional gap flow solutions. (a) p, u, w dependence on x, z produced by (5.5)–(5.6b), for rectangular planform $k = B$ (see Figure 7), $0 < x < 1$, with an oncoming (relative) wind velocity 1 at angle of incidence α to the x-axis. Here $B = \frac{1}{2}, \alpha = -25$ degrees. The undertray shape has $f(x)/h = 1 - \Gamma_1 x(1-x)^2 z^2 (B-z)^2$ with $\Gamma_1 = 30/B^4$.

$x + h^{-1}\phi_2$, (5.5) reduces to Poisson's equation $(\partial^2/\partial x^2 + \partial^2/\partial z^2)\phi_2 = -\partial f_2/\partial x$ for ϕ_2, subject to $\partial\phi_2/\partial x = 0$ at outflow edges and $\phi_2 = 0$ at inflow edges from (5.6a,b). For an underbody shape f which is not near-uniform, computations of (5.5)–(5.6b) are usually required; as one example, Figure 8(a) shows the solutions for the induced pressure p and velocities u, w as function of x, z with f given in the caption and a 25° angle of incidence.

Configurations of interest include the following four. (i) is for a wide planform where the spanwise variation is relatively weak, so that approximately (5.5) leaves fu as a function of z which is, from (5.6a), f(x_T, z), yielding u at the leading edge as $f(x_T, z)/f(x_L, z)$, in line with (4.2b). (ii) has a narrow planform, with enhanced spanwise variation. (iii) is for a near-uniform underbody shape (see ϕ_2 above) with a rectangular planform, and (iv) is as (iii) except that the spanwise dependence is periodic, as for a ribbed underbody. Configuration (i) is covered effectively by Section 4, while (iii),(iv) are found to yield physically sensible linear solutions, and an example of (ii) where the system (5.5)–(5.6b) becomes parabolized [the

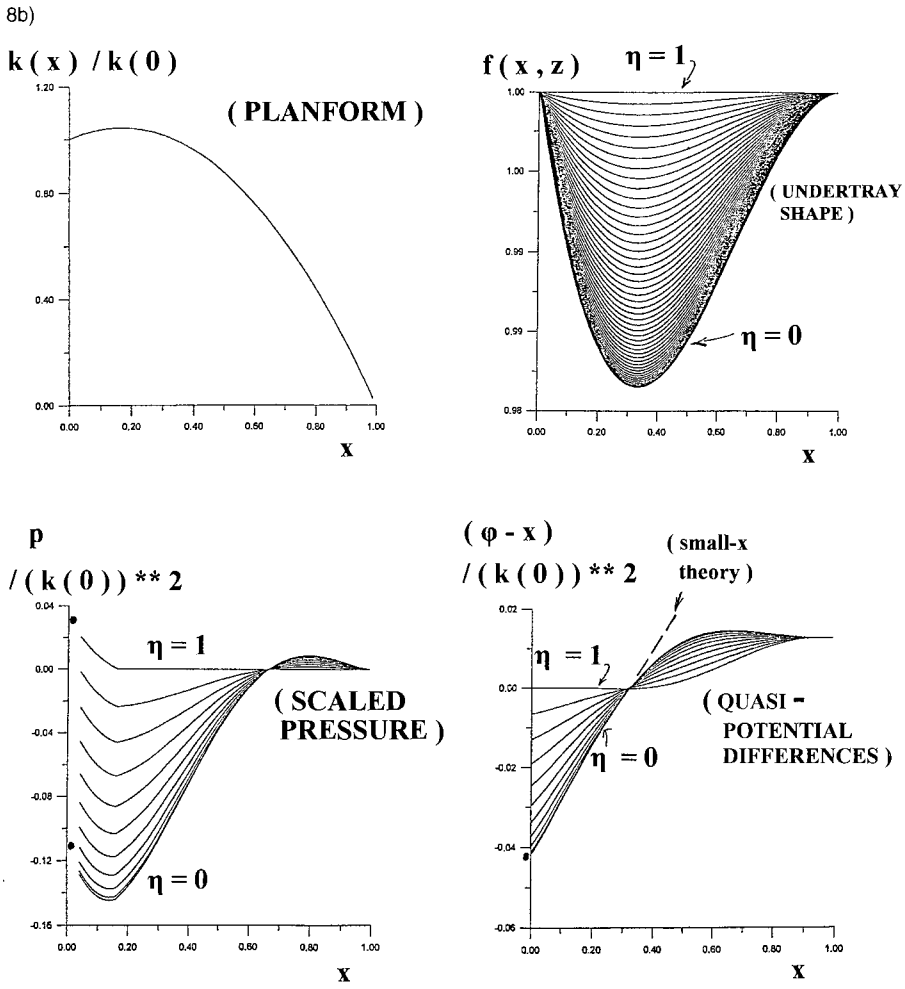

Figure 8. Computed three-dimensional gap flow solutions. (b) Scaled pressure and quasi-potential difference $(\phi - x)$, for narrow configuration (ii) of Section 5.2, with planform and undertray shape as shown and η denoting z/k. Dots and dashes indicate analytical results at small x.

first terms in (5.5),(5.6a) are replaced by $\partial f/\partial x,\ 2\partial\phi/\partial x - 1$ respectively, while the inflow-outflow switch becomes explicit near the planform tips] is presented in Figure 8(b). This figure shows the prescribed planform shape, the underbody shape, the scaled induced pressure solution and the difference function $\phi - x$, in turn, for one example of the configuration (ii). Asymptotes obtained for small x are included for comparison. The changes in boundary conditions are evident in both the pressure and the $(\phi - x)$ solutions. These solutions are in addition to the fuller nonlinear case (5.5)–(5.6b) given in Figure 8(a). In each case the leading edges are wedge-like.

Three-dimensional flow solutions for small h can also be derived analogous with those in Section 4, provided that the edge conditions in (5.3d),(5.4) continue to hold.

6. Further comments

Mechanisms. The theory and results here show that there are several important physical mechanisms to accommodate in treating undertray flows and ground effects. Some are mechanisms peculiar to these confined flows. In two-dimensional motions the mechanisms are as listed in section 1, supplemented by the wake back-effect on the gap flow due to the viscous-inviscid trailing edge requirements of local forward flow in Section 5.1 when gap-flow separation occurs. We would add two further points to this: one, that the moving surface (ground) tends to suppress separation near the leading edge (see also Appendix A); two, that the alternative design problem, of finding an undertray shape to produce a given pressure distribution, should be well-posed by (2.2a,b),(2.3a–d), (2.5) if there is no flow reversal but otherwise needs numerical care to avoid a separation singularity. Design to optimize the downforce for a restricted geometry, shown in Figure 5, is considered in appendix B and taken further by [10]. In three-dimensional motions, additional flow mechanisms arise. These relate primarily to the distinguishing (unknown in advance for aligned edges) between inflow and outflow boundary conditions at any position along the planform edge, the new form of the leading edge (inflow) jump conditions themselves, and the extra upstream influence inherent in any three-dimensional interactive boundary layer.

Three-dimensional flows. In the gap, the three-dimensional motions are understood satisfactorily (Section 5.2); a study springing from the present work is in [32, Chapter 7]. The remaining difficult issues are on the presence of concentrated edge vortices, which can alter the (otherwise consistent) leading- and trailing- edge constraints. It remains to be seen whether satisfactory modelling of wheels can be incorporated, perhaps as singularities near the edges. The solutions can also be extended to other undertray shapes, non-alignment, fuller nonlinearity, and separations in principle, for example as in the two-dimensional setting with f-effective. That is either for extreme scaled thickness h, particularly the range of large values which is currently the more realistic (see Section 1) and yields (5.5)–(5.6b), or for the more general, unified, case of $h \sim 1$ controlled by (5.2a–c) with (5.3a–d), (5.4). Numerical methods are being re-considered for this last task, results of which can be checked against those from the extremal analysis above and in Figure 8.

Turbulent flows. Further study is also required for turbulent flows in practice; see initial comments in Section 1. The laminar separations captured in the present work are likely to be very unstable, and likewise for other regions of inflectional velocity profiles (see recent studies by [33,34]), such that any unsteadiness leads readily to transition to turbulence. This in turn tends to increase the thickness factor δ as described in Section 1, despite the suppression of separation in turbulent flow. The beginnings of a (modelled) turbulent planar-mean-flow account can be seen *first* with the gap width H assumed to be comparable with δ, just as in Section 2, but δ now being larger, of order u_τ. Here u_τ is the usual turbulent wall-stress velocity in nondimensional form [35, Chapter 6],]36,37] and is typically of order $1/\log(\mathrm{Re})$. The numerical estimates in Section 1 rather favour this scale. The majority of the gap flow in region I is then analogous with the outer small-deficit layer of the two-tiered turbulent boundary layer and has

$$u = u_e(x) + u_\tau \tilde{u} + \ldots \tag{6.1}$$

[38–41], instead of (2.1). The coordinate $\tilde{y}$ now corresponds to this deficit-layer scaling. The controlling equations are the continuity equation and

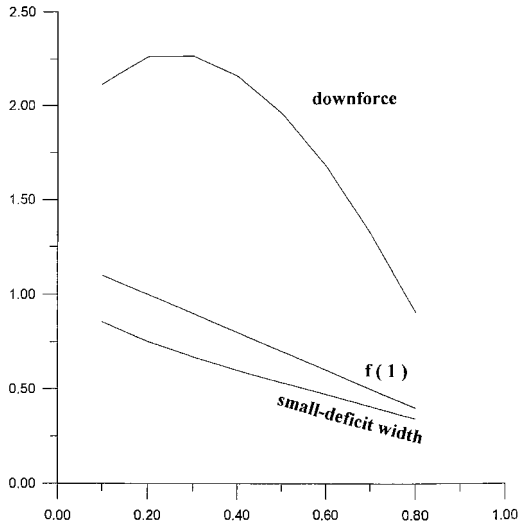

Figure 9. Turbulent-modelled results based on (6.1)–(6.2) with $u_\tau = 0{\cdot}2$, showing dependence of downforce, end-gap width $f(1)$ and width of small-deficit layer on junction position ℓ, for fixed slope $(r-1)h/(1-\ell)$ of 1, with same geometry as in figure 5 and $h = 0{\cdot}2$.

$$u_e \frac{\partial \tilde{u}}{\partial x} + \tilde{u} u_e' - \tilde{y} u_e' \frac{\partial \tilde{u}}{\partial \tilde{y}} = T, \tag{6.2}$$

subject to logarithmic matching conditions near the ground and the undersurface, such that we presume $\tilde{u}$ behaves as $(u_e - u_W)\log\tilde{y}$ at small positive $\tilde{y}$ and $u_e \log(f - \tilde{y})$ at small positive $f - \tilde{y}$, in turn. Here the turbulent stress acts through the term $T = \partial(B\partial\tilde{u}/\partial\tilde{y})/\partial\tilde{y}$, in a mixing-length form such as in the Cebeci-Smith model, while the u_W logarithmic term seems necessary for the moving ground condition (here u_W is unity). A three-tiered definition of B can apply to this model by analogy with unconfined motion, with a tier near each solid surface and one tier in between, and continuity of B, $\partial u/\partial y$, u is then required at the unknown junctions between the tiers. See also [42,43]. There are also extremely thin laminar-turbulent-stress sublayers of thickness $0(\mathrm{Re}^{-1}u_\tau^{-1})$ close to the ground and undersurface, to attain the velocities $(u_W, 0)$, $(0, 0)$ respectively, but they are of no direct concern here provided that subtle effects as for surface injection [44,45] do not arise from them. The solution of (6.2) can be derived in principle, together with the logarithmic conditions and the mass-flux and streamwise-edge constraints as in Sections 2–5, for a specified mixing-length model. The central point, however, is that the velocity profile in (6.1) is independent of $\tilde{y}$ to leading approximation and $u_e(x)$, $p(x)$ must therefore be governed by inviscid thin-gap theory exactly as for the large-h extreme of *laminar* flow, in (4.2a,b) for two-dimensional and (5.5)–(5.6b) for three-dimensional motions. Hence the results there cross over *precisely* to this more realistic case. The same conclusion applies to the basic mechanisms such as leading-edge jumps, viscous-inviscid interaction, moving ground effects, present at either leading or second order.

Against that, in practice u_τ is significant (approximately 0.1 to 0.2 for example) and effects from the deficit contribution $\tilde{u}$ do matter substantially. Computational results incorporating the latter effects are given in Figure 9, for the front-flap shapes discussed in Appendix B. The results show the lift, or rather the downforce, in the same nondimensional form as for Figures 4,5 and the relative thicknesses of the gap and of the small-deficit layer at the trailing edge. With prescribed flap slope at the rear the turbulent-modelled and laminar-flow trends are

the same, and the optimal positions of junctions are at 20–30% chord in both cases, although the downforce is found to increase monotonically with increasing slope in the turbulent case.

For narrower gaps (again we refer to the turbulence estimate in Section 1), *second*, such that the inertia forces become secondary, the composite system

$$p'(x) = T + \mathrm{Re}^{-1}\frac{\partial^2 u}{\partial y^2} \tag{6.3}$$

is more appropriate, for the total turbulent mean velocity u. This is in order to cover a wide range of small gap scalings. The characteristic pressure response here is large. Integration of (6.3) gives, with τ now standing for $\partial u/\partial y$,

$$B\tau + \mathrm{Re}^{-1}\tau = yp'(x) + D, \tag{6.4}$$

where D is an unknown function of x. Ignoring for such small gaps the middle tier mentioned above, we have unknowns $D^{\pm}(x)$ in the two tiers ($\pm$) where $y_1 < y \leqslant f$, $0 \leqslant y < y_1$ in turn, with $f(x)$ scaled and the junction $y_1(x)$ unknown. In a Cebeci-Smith model for instance where $B = y^2\{1 - \exp(-a_4 \mathrm{Re}\, u_\tau y)\}\,|\tau|$ in the $-$tier, a_4 is an 0(1) constant, and $(f - y)$ replaces y in the + tier, y_1 is found to equal $f/2$, the exponential term being negligible except for unrealistically tiny gaps; then (6.4) yields a quadratic equation for $\tau^{\pm}$ and hence one explicit relation between $D^{\pm}$, from the junction conditions. Integration in y yields $u^{\pm}$, with the values u_W, zero at $y = 0$, f, and hence a second relation, thus fixing $D^{\pm}(x)$ for given $p'(x)$. Further integration in y then provides the mass flux to be equated with hu_0, as in section 2, to determine $p'(x)$, followed by (2.3d) at the trailing edge and a leading-edge condition to fix the constant u_0. This is similar to the *laminar* case, specifically to (4.3a,b) in two dimensions and similarly in three dimensions. It would be interesting to pursue further this account, and that in (6.1)–(6.2), given the similarities between the laminar and turbulent cases together with the numerical estimates from Section 1.

Other points. Thicker bodies also need investigation, as the discussion on configurations (i)–(iv) at the beginning of Section 2 indicates, and they may well lead to larger-scale separations outside the undertray-to-ground gap. Yet the present gap-flow findings remain valid as long as the upperbody flow II is not excessively separated or subjected to a blunt trailing edge closure, and even with larger separations taking place outside the effect on the gap flow may simply be represented by a modification of the end condition (2.3d) among others, for example making $p(1)$ nonzero.

A final question is which parts of the present work apply to a representative racing car and which to a normal road car? The former have the scaled gap parameter h being much smaller, typically of order unity or not especially large, whereas the normal car has h being very large, as described in the introduction. The differences can thus be seen in Figures 2(b), 2(c), and in the h-dependence demonstrated in Figure 4, as well as in the analyses for large h values in Section 4,5. The increased downforce possible for the typical racing car value of h is evident in Figure 4. That is for laminar flow. In the turbulent case the differences continue although they are less marked according to the comments in the introduction and earlier in this section. Again, experimental measurements (kindly brought to our attention by Professor S. Bhattacharyya after this work was completed) on a wing in ground effect are given in [46]; see also [47]. The experimental results for pressure, lift and separation position in Figures 2,3,5,6,11 of [46] are found to agree well at least qualitatively with the theoretical ones in our Figures 4, 4 (and 9), 2(b,c), 2(b,c), 4, respectively. The crucial values of the

relative height H are about 0.1 in the experiments, thus being in line with the theoretical ones (see our Sections 1,2).

Thanks are due to Frank Coppuck and Ian Gough at McLaren Racing for illuminating discussions and comments on their and our research, to Professor S. Bhattacharyya, Professor J.C.R. Hunt, Dr. J.R. Ockendon, Mr. R. Purvis, Dr. S.N. Timoshin, Dr. L. Townend and the referees for their interest and constructive comments, and to EPSRC for support of M.A.J.

Appendix A. Local leading-edge solution

In order to find Ψ (see in the text after (2.4)) we write it in the form

$$\Psi(\tilde{x}, \tilde{y}) = \tilde{y} + \psi(\tilde{x}, \tilde{y}), \tag{A1}$$

where ψ also satisfies Laplace's equation and the boundary conditions

$$\psi(\tilde{x}, 0) = 0, \tag{A2}$$

$$\psi(\tilde{x}, h) = \Psi_0 - h \quad \text{for} \quad \tilde{x} \geq 0, \tag{A3}$$

and $\psi(\tilde{x}, \tilde{y})$ approaches zero in the farfield outside the gap.

We find ψ by introducing the complex variables $z = \tilde{x} + i\tilde{y}$ and $\zeta = \xi + i\eta$ and using a conformal mapping technique. To obtain the desired solution in the z-plane we map the relevant uniform channel flow in the ζ-plane, for which the streamfunction is given by $\psi = (\Psi_0 - h)\,\eta$, back onto the leading edge geometry (z-plane) using the conformal mapping

$$z = h\left(\zeta - \frac{1}{\pi}\left(1 + e^{-\pi\zeta}\right)\right). \tag{A4}$$

This conformal mapping is non-invertible and therefore we may only define $\psi(\tilde{x}, \tilde{y})$, and hence the solution $\Psi(\tilde{x}, \tilde{y})$, implicitly using ξ and η.

For a given ξ, η we have

$$\Psi = \tilde{y} + (\Psi_0 - h)\,\eta, \tag{A5}$$

$$\tilde{x} = h\left(\xi - \frac{1}{\pi}\left(1 + e^{-\pi\xi}\cos\pi\eta\right)\right), \tag{A6}$$

$$\tilde{y} = h\left(\eta + \frac{1}{\pi}e^{-\pi\xi}\sin\pi\eta\right). \tag{A7}$$

The complex velocity is given by

$$U - iV = 1 + \frac{(\Psi_0 - h)}{h\left(1 + e^{-\pi(\xi + i\eta)}\right)}. \tag{A8}$$

As we move into the gap, $\xi \to +\infty$, $U \to \Psi_0/h$, $V \to 0$, whereas in the farfield outside the gap $\xi \to -\infty$, $U \to 1$, $V \to 0$ as required. Therefore by Bernoulli's theorem the pressure must jump from zero upstream of the leading edge region to $\frac{1}{2}\left(1 - \left(\frac{\Psi_0}{h}\right)^2\right)$ just downstream of the leading edge region inside the gap.

Appendix B. Optimisation of undertray shape design with regard to downforce production

In discussion with McLaren Motorsport we investigated the effects of undertray shape design on downforce production with reference to the front flap on a Formula 1 racing car. To start with we decided on a simple piecewise linear design for the undertray shape described by the function

$$f_1(x) = \left\{ \begin{array}{ll} h & \text{for} \quad x \in [0, \ell] \\ h\left(r + \dfrac{(1-r)}{(1-\ell)}(1-x)\right) & \text{for} \quad x \in [\ell, 1] \end{array} \right\}. \tag{B1}$$

The diffuser has a minimum ground clearance of h and a horizontal channel throat of length ℓ followed by a linearly expanding region with maximum ground clearance rh at $x = 1$, that is, at the trailing edge.

The lift produced by this undertray design, with h fixed, was calculated as part of a numerical boundary-layer solution for a range of values of ℓ, r. Fig.5 shows the lift L plotted as a function of ℓ, r for $h = 1$ and clearly identifies a minimum lift configuration with $L = -0{\cdot}15$, $\ell = 0{\cdot}15$, and $r = 2{\cdot}55$. For constant h, ℓ the lift decreases with increasing r. At some r separation occurs and, as the region of reversed flow becomes large, downforce production is inhibited and the lift begins to increase again. That leads to a minimum lift or maximum downforce configuration. This calculation required around 400 boundary layer code runs and could become prohibitively expensive as more complicated designs were proposed.

Therefore a simpler lubrication-theory approach was developed which gave an exact expression for the lift L produced by a given undertray-shape $f(x)$, namely

$$L = 6\left\langle f^{-2}\right\rangle \int_0^1 \int_0^x \left(\frac{f^{-2}(\xi)}{\left\langle f^{-2}\right\rangle} - \frac{f^{-3}(\xi)}{\left\langle f^{-3}\right\rangle} \right) \mathrm{d}\xi \, \mathrm{d}x, \tag{B2}$$

where

$$\left\langle f^{-n}\right\rangle = \int_0^1 f^{-n}(x)\, \mathrm{d}x. \tag{B3}$$

This formula is only valid for $\left\langle f^{-2}\right\rangle \gg 1$ but provides a useful investigative tool as far as designing an optimal undertray shape is concerned. For $f_1(x)$ equation (B2) gives an optimal lift of $L = -0{\cdot}1923/h^2$ with $\ell = 0{\cdot}197$, $r = 2{\cdot}24$. However (B2) does suggest that a better undertray shape would be the simple step change in height

$$f_2(x) = \left\{ \begin{array}{ll} h & \text{for} \quad x \in [0, \ell] \\ rh & \text{for} \quad x \in [\ell, 1] \end{array} \right\}. \tag{B4}$$

For $f_2(x)$ equation (B2) gives an optimal lift of $L = -0{\cdot}2063/h^2$ with $\ell = 0{\cdot}282$, $r = 1{\cdot}866$, this being a 7.25% improvement over $f_1(x)$. It should be noted that when solving the boundary layer equations any such step change in undertray shape may have to be smoothed out over some length scale.

References

1. R.G. Dominy, The influence of slipstreaming on the performance of a Grand Prix racing car. *J. Automobile Eng. (Proc. I. Mech. Eng.)* 204 (1990) 35–40.
2. R.G. Dominy, Aerodynamics of a Grand Prix racing car. *J. Automobile Eng. (Proc. I. Mech. Eng.)* 206 (1992) 267–274.
3. P.G. Wright, The influence of aerodynamics on the design of Formula One racing cars. *Int. J. Vehicle Design* 3. (1982) 383–396.
4. J. Katz, Investigation of negative lifting surfaces attached to an open-wheel racing car configuration. *Int. Congr. & Exposition* Detroit, Michigan, Feb.25-Mar.1, SAE tech. ppr. 850283 (1985) pp. 383–396.
5. J. Katz, Calculation of the aerodynamic forces on automobile lifting surfaces. *J. Fluids Eng., Trans. A.S.M.E.* 107 (1985) 438–443.
6. K. Jacob, Advanced method for computing flow around wings with rear separation and ground effect. *J. Aircraft* 24 (1986) 126–128.
7. Y.B. Suh. and C. Ostowari, Drag reduction factor due to ground effect. *J. Aircraft* 25 (1988) 1071–1072.
8. P.W. Bearman, Bluff body flows applicable to vehicle aerodynamics. In: T. Morel and C. Dalton (eds.), *Aerodynamics of Transportation*. New York: A.S.M.E., (1980) pp. 265–274.
9. M.D. Chawla, L.C. Edwards and M.E. Franke, Wind-tunnel investigation of wing-in-ground effects. *J. Aircraft* 27 (1990) 289–293.
10. M.A. Jones, Mechanisms in Wing-in-Ground Effect Aerodynamics. *Ph.D. thesis*. Univ. of London (2000) 210 pp.
11. S.E. Widnall and T.M. Barrows, An analytical solution for two- and three-dimensional wings in ground effect. *J. Fluid Mech*. 41 (1970) 769–792.
12. J.N. Newman, Analysis of small-aspect-ratio lifting surfaces in ground effect. *J. Fluid Mech.* 117 (1982) 305–314.
13. E.O. Tuck and M. Bentwich, Sliding sheets: lubrication with comparable viscous and inertia forces. *J. Fluid Mech*. 135 (1983) 51–69.
14. A.Z. Szeri, Some extensions of the lubrication theory of Osborne Reynolds. *J. Tribology, Trans. A.S.M.E*. 109 (1987) 21–36.
15. J.A. Tichy, Entry flow in a narrow channel of varying gap with one sliding surface. *J. Tribology, Trans. A.S.M.E*. 108 (1986) 288–293.
16. A. Plotkin and S.S. Dodbele, Slender wing in ground effect. *A.I.A.A. J. Tech. Note*. 26 (1988) 493–494.
17. S.K. Wilson and B.R. Duffy, On lubrication with comparable viscous and inertia forces. *Quart. J. Mech. Applied Maths*. 51 (1998) 105–124.
18. O.E. Jensen, The stress singularity in surfactant-driven thin-film flows. Part 2. Inertial effects. *J. Fluid Mech.* 372 (1998) 301–322.
19. F.T. Smith, Flow through symmetrically constricted tubes. *J. Inst. Maths. Applics*. 21 (1978) 145–156.
20. F.T. Smith and P.W. Duck, On the severe nonsymmetric constriction, curving or cornering of channel flows. *J. Fluid Mech.* 90 (1980) 727–753.
21. F. Ernst and M. Perić, *Kombinierte experimentall-numerische Strömungsuntersuchungen an einen zwei-dimensionelen Fahrzeungmodell.* LSTM Bericht 182/I/87, Lehrstuhl für Stromungsmechanik, Univ. Erlangen-Nürnberg, Germany (1987) 37 pp.
22. F.T. Smith, On physical mechanisms in two- and three-dimensional separations. *Phil. Trans. R. Soc. London A (theme issue)* 358 (2000) 3091–3111.
23. F.T. Smith and M.A. Jones, One-to-few and one-to-many branching tube flows. *J. Fluid Mech.* 423 (2000) 1–31.
24. R.G.A. Bowles and F.T. Smith, Lifting multi-blade flows with interaction. *J. Fluid Mech*. 415 (2000) 203–226.
25. F.T. Smith and S.N. Timoshin, Blade-wake interactions and rotary boundary layers. *Proc. R. Soc. Lond. A* 452 (1996) 1301–1329.
26. F.T. Smith and S.N. Timoshin, Planar flows past thin multi-blade configurations. *J. Fluid Mech.* 324 (1996) 355–377.
27. F.T. Smith, Boundary layer flow near a discontinuity in wall conditions. *J. Inst. Maths. Applics.* 13 (1974) 127–145.

28. F.T. Smith and P.G. Daniels, Removal of Goldstein's singularity at separation in flow past obstacles in wall layers. *J. Fluid Mech.* 110 (1981) 1–37.
29. F.T. Smith, Interacting flow theory and trailing edge separation - no stall. *J. Fluid Mech.* 131 (1983) 219–249.
30. F.T. Smith, Pipeflows distorted by non-symmetric indentation or branching. *Mathematika* 23 (1976) 62–83.
31. R.I. Sykes, On three-dimensional boundary layer flow over surface irregularities. *Proc. R. Soc. London A* 373 (1980) 311–329.
32. R. Purvis, Rotor Blades and Ground Effect. *Ph.D. thesis*, University of London (2002) 230 pp.
33. L. Li, J.D.A. Walker, R. Bowles and F.T. Smith, Short-scale break-up in unsteady interactive layers: local development of normal pressure gradients and vortex wind-up. *J. Fluid Mech.* 374 (1998) 335–378.
34. D.J. Savin, F.T. Smith and T. Allen, Transition of free disturbances in inflectional flow over an isolated surface roughness. *Proc. R. Soc. London A* 455 (1999) 491–541.
35. T. Cebeci and A.M.O. Smith, *Analysis of Turbulent Boundary Layers.* New York: Academic Press (1974) 404 pp.
36. R.I. Sykes, An asymptotic theory of incompressible turbulent boundary-layer flow over a small hump. *J. Fluid Mech.* 101 (1980) 647–670.
37. P. Bradshaw, Prediction of the turbulent near-wake of a symmetrical airfoil. *A.I.A.A. J.* 8 (1970) 1507–1512.
38. G.L. Mellor, The large Reynolds number, asymptotic theory of turbulent boundary layers. *Int. J. Eng. Sci.* 10 (1972) 851–873.
39. W.B. Bush and F.E. Fendell, Asymptotic analysis of turbulent channel and boundary-layer flow. *J. Fluid Mech.* 56 (1972) 657–681.
40. A. Neish and F.T. Smith, On turbulent separation in the flow past a bluff body. *J. Fluid Mech.* 241 (1992) 443–467.
41. A.T. Degani, F.T. Smith and J.D.A. Walker, The structure of a three-dimensional turbulent boundary layer. *J. Fluid Mech.* 250 (1993) 43–68.
42. G.I. Taylor, The dispersion of matter in turbulent flow through a pipe. *Proc. R. Soc. London A* 233 (1954) 446–468.
43. A. Purnama, Boundary retention effects upon contaminant dispersion in parallel flows. *J. Fluid Mech.* 195 (1988) 393–412.
44. A. Silva-Freires, An Asymptotic Approach for Shock Wave/Turbulent Boundary Layer Interaction. *Ph.D. thesis*, University of Cambridge (1990) 245 pp.
45. F.T. Smith and S.N. Timoshin, Vortex-generator jets: theoretical prediction and design. *Utd. Techn. Res. Cent. report.* UTRC94-93, East Hartford, CT, USA (1994) 32 pp.
46. J. Zerihan and X. Zhian, Aerodynamics of a single element wing in ground effect. *J. Aircraft* 37 (2000) 1058–1064.
47. J. Zerihan and X. Zhang, Aerodynamics of Gurney flaps on a wing in ground effect. *AIAA J.* 39 (2001) 772–780.